Chinese Chemical Letters 33 (2022) 3249–3254

Contents lists available at ScienceDirect

Chinese Chemical Letters

journal homepage: www.elsevier.com/locate/cclet

A controllable preparation of two-dimensional cobalt oxalate-based nanostructured sheets for electrochemical energy storage

Fancheng Sun, Qing Li, Yang Bai, Guangxun Zhang, Shasha Zheng, Maoying Peng, Xudong Chen, Nuo Lin, Huan Pang*

School of Chemistry and Chemical Engineering, Institute for Innovative Materials and Energy, Yangzhou University, Yangzhou 225009, China

ARTICLE INFO

Article history:
Received 15 August 2021
Revised 16 October 2021
Accepted 26 October 2021
Available online 29 October 2021

Keywords:
Two-dimensional nanosheets
Cobalt oxalate
Co_3O_4
Energy storage
Capacity

ABSTRACT

Well-defined two-dimensional (2D) cobalt oxalate ($CoC_2O_4·2H_2O$) nanosheets exhibit more excellent property than common bulk cobalt oxalate due to high specific surface areas and high-efficient transport of ion and electron. However, the delicate control of the 2D morphology of $CoC_2O_4·2H_2O$ during their synthesis remains challenging. Herein, 2D $CoC_2O_4·2H_2O$ nanosheets (M1), grown by straightforward chemical precipitation, can be tuned from three-dimensional (3D) structure during their synthesis with no templates or capping agents. This control is obtained by rationally changing the ratio of reactants with ethylene glycol as solvent. Moreover, Co_3O_4/CoC_2O_4 composites (M1-250) have been fabricated through low-temperature thermal treatment of the M1 precursor in air, which possess porous surfaces with the 2D morphology maintained. Benefiting from the porous surfaces, more redox-active sites and better electrical conductivity of Co_3O_4, the constructed M1-250//AC aqueous device manifest improved kinetics of the electrochemistry process with energy density of 27.9 Wh/kg at 550.7 W/kg and good cycling stability with sustaining 73.0 mAh/g after 5000 cycles.

To fulfil the requirements of practical applications in a variety of electrochemical energy storage devices, such as asymmetric supercapacitors, research efforts have been directed made towards finding multifunctional inorganic materials with specific micro/nanoscopic morphologies [1–6]. As the surface energy, chemical reactivity and electronic structure of inorganic materials are closely related to the surface morphology [7–10], fine-tuning of the surface structure and morphology of the material at the micro/nanoscale will be in favor of improving their performance and endowing the material new functions [11–16]. For example, for noble metal nanoparticles, as the size decreases, the surface energy becomes higher and the catalytic activity will be greatly improved [17]. The essence of morphology control is to regulate the formation of micro/nanomaterials with different exposed crystal planes [18,19]. However, seeking an effective and facile approach to adjust the chemical and physical characteristics of micro/nanomaterials in terms of size and shape still remains challenging.

Two dimensional (2D) nanomaterials with large specific surface areas and similar sheet-like morphologies, such as layered double hydroxides [20], graphene and its derivatives [21], transition metal dichalcogenides [22], graphitic carbon nitride [23], have received considerable attentions owing to efficient transport of ion and electron, as well as better adaption to structural alteration in the electrochemical process, showing enormous potential in energy storage devices. Recently, many researches about 2D transition metal oxalate nanomaterials have found that compared with their bulk counterparts, these materials have great application potential as electrode materials for supercapacitors owing to larger reversible specific capacities [24,25]. Specifically, many methods have been utilized for synthesizing 2D nanomaterials, such as top-down methods including exfoliation of bulk materials using different solvents [26], and bottom-up methods including interfacial synthesis [20], hydrothermal strategy [24], in which top-down methods have the disadvantage of time-consuming and low-yield. Significantly, the selection of solvent with specific physical/chemical properties has important influences on the controllable synthesis of micro/nanomaterials, including the size and dimension [27–31]. On one hand, solvent molecules act an important role in regulating the process of thermodynamic assembly [32,33], including changing the self-assembly pattern of solute molecules by interaction of solute and solvent, and affecting the crystallization process and solubility of solute molecules. On the other hand, solvent can participate in the chemical reaction process through multiple weak interactions, such as Van der Waals force, dipole-dipole interaction force and hydrogen bonding force, which have a great impact on

* Corresponding author.
E-mail addresses: huanpangchem@hotmail.com, panghuan@yzu.edu.cn (H. Pang).

https://doi.org/10.1016/j.cclet.2021.10.075
1001-8417/

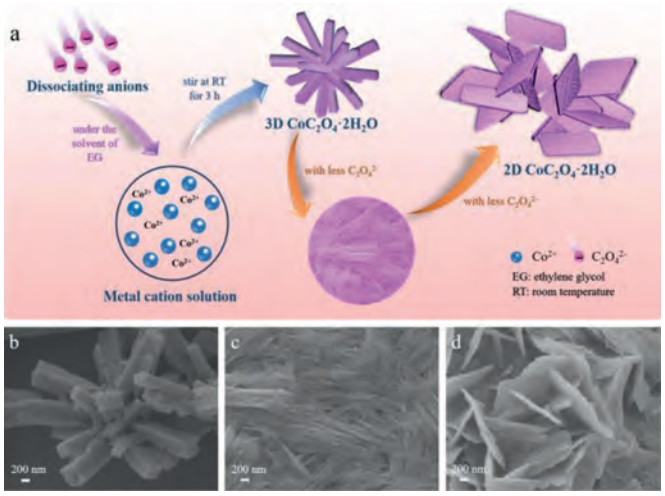

Fig. 1. (a) Schematic illustration of the morphology growth trend of 2D $CoC_2O_4·2H_2O$ under EG solvent. SEM images of $CoC_2O_4·2H_2O$ with different morphologies. The specific molar ration of $Co(Ac)_2·4H_2O$ to $(NH_4)_2C_2O_4·H_2O$ of (b) 1:5, (c) 1:1, (d) 5:1.

the reaction system [34,35]. Therefore, it is of great potential application value to utilize solvent effect on the regulation of 2D materials.

Herein, we propose a facile approach to fabricating 2D nanostructured cobalt oxalate-based electrode materials with large specific capacity as well as exceptional cycling stability, by judiciously formulating initial reactants ratio under solvent of ethylene glycol (EG). Specifically, 2D uniform $CoC_2O_4·2H_2O$ nanosheets (M1) were prepared via room temperature precipitation, which could be tuned with an optimized ratio of cobalt(II) acetate tetrahydrate and ammonium oxalate monohydrate in the solvent of EG. Meanwhile, the growth process of sheet-like M1 in the solvent of EG was studied. It is well known that the growth method of straightforward precipitation process is a widely-used process to get various inorganic materials, however the consequent high-speed reaction rates make it hard to achieve precise morphology control [9]. Here the selected solvent EG acted a significant factor in adjusting the reaction rates and the morphologies, as well as the crystallite nucleation and growth kinetics. The subsequent low-temperature thermal transformation treatment converted the precursor (M1) to the target electrode material, Co_3O_4/CoC_2O_4 composites (M1-250), with an overall conservation of morphology. Benefiting from the porous surfaces, more redox-active sites and better conductivity of Co_3O_4, the constructed M1-250//AC aqueous device manifested improved kinetics of the electrochemistry process with a specific capacity of 53.3 mAh/g at 0.5 A/g, energy density of 27.9 Wh/kg at 550.7 W/kg and good cycling stability (sustaining 73.0 mAh/g after 5000 cycles). This work emphasizes the facile approach for the fabrication of cobalt oxalate-based nanosheets and its high efficiency as electrode materials for energy storage devices.

Fig. 1a delineates our strategy for generating 2D uniform $CoC_2O_4·2H_2O$ nanosheets (M1), involving a precipitation step at room temperature mediated by changing the initial reactants ratio to decrease the concentration of $C_2O_4^{2-}$ ion under the solvent of EG, without any use of surfactant. At a high $(NH_4)_2C_2O_4$-EG solution volume ratio (83%), the morphology of the product M5 is 3D cuboid-like (Fig. 1b). Decreasing the solution volume ratio $(NH_4)_2C_2O_4$-EG to 50% obtains sample M3 (Fig. 1c), which does not show any specific morphology. When the solution volume ratio $(NH_4)_2C_2O_4$-EG is further decreased to 17%, the SEM image of obtained M1 (Fig. 1d and Fig. S1 in Supporting information) displays 2D sheet-like morphology with relatively flat surface. Significantly, different reactants ratio has an effect on the grown direction [36]. In short, uniform 2D M1 nanosheets can only be obtained with a certain initial reactants ratio in the solvent of EG, which could be tuned from 3D $CoC_2O_4·2H_2O$ (M5) with a certain reactants ratio of $Co(Ac)_2·4H_2O$ and $(NH_4)_2C_2O_4·H_2O$ changing from 1:5 to 5:1, means the concentration decrease of $C_2O_4^{2-}$ ion.

In all synthesis process, we chose $Co(Ac)_2·4H_2O$ and $(NH_4)_2C_2O_4·H_2O$ as reactants, both of which were strong electrolytes. For dissociation equilibrium:

$$\alpha = \frac{C_{DA}}{C_R} \quad (1)$$

where α represents the electrolytic dissociation; C_{DA} stands for the concentration of dissociated reactant anions; C_R stands for the concentration of the reactant. For strong electrolytes, $\alpha \approx 1$, which can release sufficient ions instantly, and nucleate and precipitate at a high rate. Therefore, when we used deionized water as solvent, the reaction system became turbid rapidly. And by using SEM investigation, 3D large size structures of $CoC_2O_4·2H_2O$ under deionized water solvent with different initial reactants ratio (molar ratio of $Co(Ac)_2·4H_2O$ and $(NH_4)_2C_2O_4·H_2O$ were 5:1, 2:1, 1:1, 1:2, 1:5, denoted as O1–O5, respectively) were monitored (Figs. S2c1–c5 in Supporting information). Compared with using deionized water as solvent, making use of EG as solvent leads to gradual releasing of target ions, which is expected to affect and reduce the nucleation and growth kinetics. Besides, EG has a certain coordination ability, which hinders the reaction between oxalate and metal ions [37]. By utilizing SEM investigation, it can be found that when using EG as solvent, the size becomes smaller and 2D/3D micro/nanomaterials are obtained (Figs. S2a1–a5 in Supporting information, samples under EG solvent with different molar ratio of $Co(Ac)_2·4H_2O$ and $(NH_4)_2C_2O_4·H_2O$, 5:1, 2:1, 1:1, 1:2, 1:5, were denoted as M1–M5, respectively). An interesting phenomenon was that when the products with EG as solvent were washed by deionized water (N1–N5), the color and morphology of them both changed. The color changed from purple to light pink (Fig. S3 in Supporting information) and the morphology changes to rod-like (Figs. S2b1–b5 in Supporting information). It may because that when washed by deionized water, part of the cobalt ions limited by ethylene glycol were released, which made the cobalt ions react with $C_2O_4^{2-}$ ion rapidly to form light pink cobalt oxalate precipitation.

In summary, EG solvent plays a special role in the synthesis process: (1) Compared with deionized water, EG has a higher viscosity and less fluidity, which prevents the close contact between grains and reduces the size of the product when used as a solvent. (2) EG has a certain coordination ability, which hinders the reaction between oxalate and metal ions. (3) Compared with rod-like O1-O5 which directly used deionized water as solvent, the size of N1–N5 changed.

X-ray diffraction (XRD) patterns of M1–M5 are illustrated in Fig. S4a (Supporting information). The diffraction peaks are corresponding to the $CoC_2O_4·2H_2O$ (PDF#25–0250), confirming the growth of $CoC_2O_4·2H_2O$. The characteristic peaks at 2θ = 18.75°, 21.29°, 22.72°, 29.16°, 34.98° are attributed to the reflections of (200), (112), (004), (114), (022) planes of $CoC_2O_4·2H_2O$. It is noteworthy that the samples of M series adopt similar XRD patterns except for the changed intensity and width of diffraction peaks resulted from different initial reactants ratio. Specifically, M1–M3 are crystal samples with weak diffraction peaks and M4–M5 samples have clear diffraction peaks. Meanwhile, Fourier transform-infrared radiation (FT-IR) spectrum indicates the existence of $CoC_2O_4·2H_2O$ (Fig. S4b in Supporting information). In detail, these complexes illustrate six vibrational bands at 3380, 1625, 1359, 1317, 825 and 490 cm^{-1}, corresponding to ν(O–H), ν_{as}(C=O), ν_s(C–O), δ(O–C=O), δ(O–C=O), and Co–O vibration, respectively. As illustrated in Fig. S5 (Supporting information) and Figs. 3f–h, the X-ray photoelectron

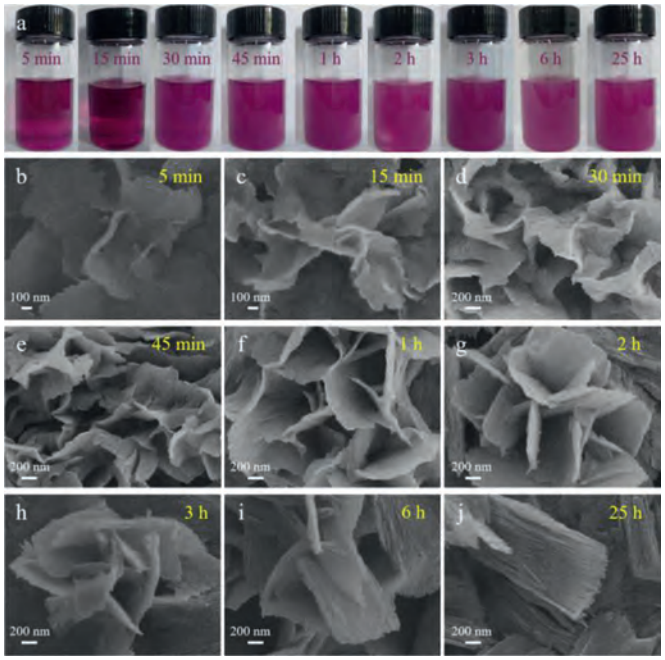

Fig. 2. (a) Digital photographs of sheet-like $CoC_2O_4{\cdot}2H_2O$ (M1) formed in EG solution over time. (b–j) SEM images of M1-5 min, M1-15 min, M1-30 min, M1-45 min, M1-1 h, M1-2 h, M1-3 h, M1-6 h, M1-25 h.

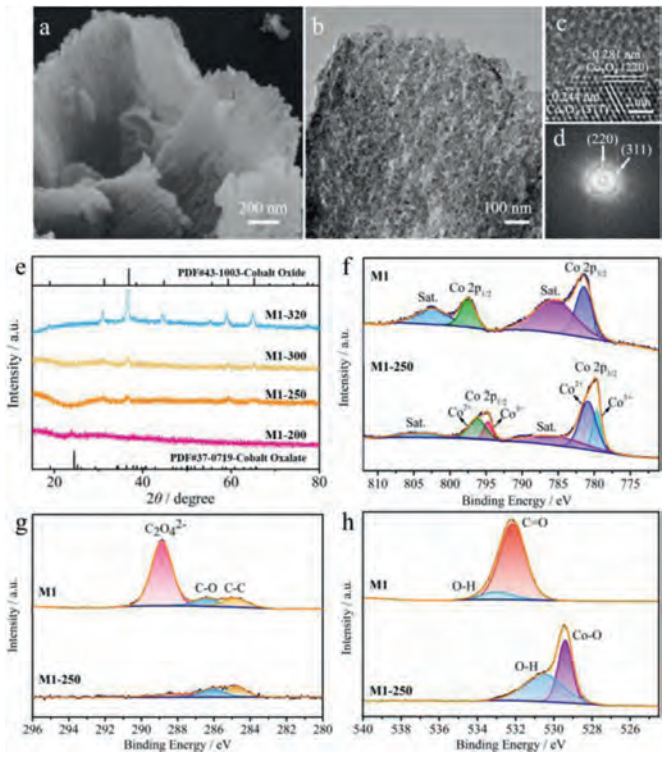

Fig. 3. (a) SEM image, (b) TEM image, (c) HRTEM image and (d) corresponding FFT pattern of M1-250. (e) XRD patterns of M1-200, M1-250, M1-300, M1-320. High resolution (f) Co 2p, (g) C 1s and (h) O 1s XPS spectra of M1 and M1-250.

spectroscopy (XPS) spectra of M1 prove the existence of cobalt, carbon and oxygen elements. The binding energy difference between Co $2p_{3/2}$ and Co $2p_{1/2}$ is 16 eV, indicating Co(II) state in M1 [38].

To further understand the formation process of sheet-like M1, time-dependent experiments in EG solvent at room temperature were performed, and the morphologies of products were studied by SEM (Fig. 2). As illustrated in Fig. 2a, the reacting mixtures became opaque with the increase of reaction time. When a sample was taken promptly after 5 min of reaction, the collected product appeared sheet-like structures with irregular flakes (Fig. 2b); With the increase of reaction time, irregular flakes gradually grown into regular rectangular thin flakes and aggregated (Figs. 2c–j). After 2 h of reaction, the morphology of the rectangular sheet barely changed, but the surface became rough. Such 2D nanosheet structure could facilitate efficient transport of ion and electron, and have great research and application potential in energy storage devices [39].

Thermal gravity (TG) analysis of M1 indicates that a major weight loss (39.8%) occur at about 300 °C, which refers to the decomposition of cobalt oxalate (Fig. S6 in Supporting information). The product annealed at 250 °C for 2 h (defined as M1-250) is indexable as a Co_3O_4/CoC_2O_4 composite (Figs. 3a and b). For comparison, the other three thermal treatment temperatures of M1 are selected at 200 °C (M1-200), 300 °C (M1-300) and 320 °C (M1-320), respectively. The color of the samples changes from flesh-colored (M1), purple (M1-200) to black (M1-250, M1-300 and M1-320) (Fig. S7 in Supporting information). Among them, M1-200 (Figs. S8a1–a2 in Supporting information), M1-250 (Figs. S8b1–b2 in Supporting information) as well as M1-300 (Figs. S8c1–c2 in Supporting information) can retain the sheet-like morphology, while the morphology of M1-320 (Figs. S8d1 and d2 in Supporting information) break into small pieces. It can be found that with the increase of temperature, the surface of the sample change from smooth to porous, and more and more Co_3O_4 nanoparticles appear. The HRTEM image (Fig. 3c) and corresponding FFT pattern (Fig. 3d) of M1-250 verify the crystalline property of M1-250 with the lattice distance of 2.4 and 2.8 Å, match well with to the (311) and (220) planes of Co_3O_4, respectively. Energy-dispersive X-ray (EDX) spectroscopy analysis validates the existence of Co, C and O in the M1-250 with a Co/O atomic ratio around 0.40 (Fig. S9 in Supporting information). Significantly, the sample calcined at 250 °C still remains partial amorphous layer (Fig. 3c), inferring that the obtained M1-250 is the composite of CoC_2O_4 and Co_3O_4, which could be further demonstrated by XRD (Fig. 3e) and FT-IR spectra (Fig. S10 in Supporting information). In the XRD pattern of M1-250, weak characteristic peak of Co_3O_4 (at 36.8°) can be observed, which means partially formation of Co_3O_4 with poor crystallinity. Moreover, in the FT-IR spectra, it can be find that M1-250 still remain the absorption bands at around 3400 cm^{-1} and 1625 cm^{-1}, related to O–H and C=O (from oxalate) stretching vibration separately, indicating the residual functional groups on the cobalt oxalate after the calcination at 250 °C [40]. Besides, the strong absorptions at 573 and 664 cm^{-1} of M1-250 are ascribed to the Co-O vibration of spinel Co_3O_4. Collectively, TGA, XRD, and FT-IR demonstrate that the sample M1-200 removed crystal water and retain the structure of cobalt oxalate; The M1-250 and M1-300 samples were both the hybrid of CoC_2O_4/Co_3O_4, while the Co/O atomic ratio of them are different (1:2.51 for M1-250 and 1:2.37 for M1-300, Figs. S9 and S11 in Supporting information). The sample M1-320 was conformed as Co_3O_4 with enhanced crystallinity. In addition, the N_2 adsorption/desorption isotherm curves (Fig. S12 in Supporting information) possesses the typical feature of mesoporous materials. With the increase of calculation temperature, the BET surface area increases gradually. The corresponding curve of BJH pore size distribution of M1-250 suggests that the average pore size is about 13 nm (Fig. S12c). Generally speaking, a large number of mesopores can promote better electrolyte permeation to access more redox active sites. However, higher crystallinity and more exposed crystal faces with the increase of calcination temperature may have a certain impact on the transport of electrons or protons in electrochemical processes.

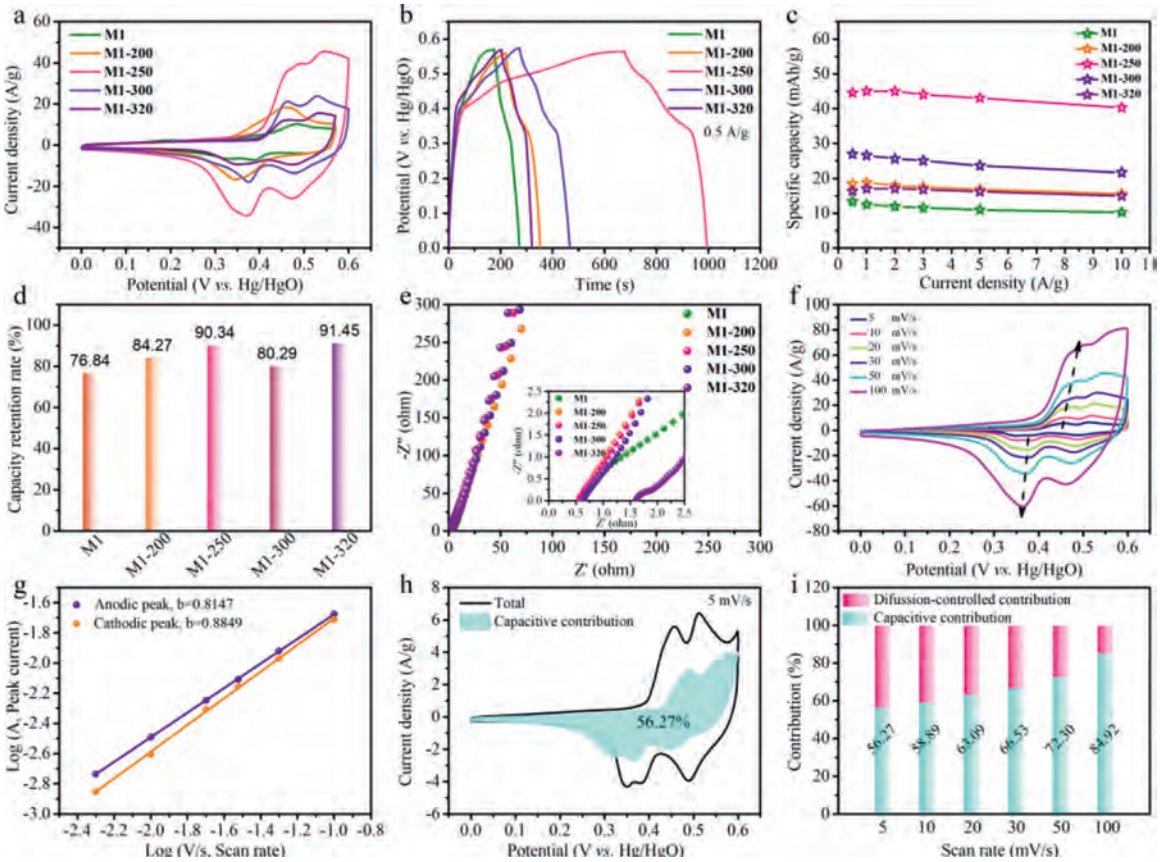

Fig. 4. Electrochemical performance of as-prepared electrodes (M1, M1-200, M1-250, M1-300, M1-320) in a three-electrode cell with 3.0 mol/L KOH aqueous electrolyte. (a) CV curves at 50 mV/s. (b) GCD curves at 0.5 A/g. (c) The specific capacity at various current densities (from 0.5 A/g to 10 A/g). (d) The retention rates of specific capacity when the current density increased from 0.5 A/g to 10 A/g. (e) The electrochemical impedance (EIS) spectra at room temperature, the insert shows the enlarged plots. (f) CV curves of M1-250 electrode at different scan rates. (g) The plots of log(peak current) against log(scan rate) for M1-250 electrode. (h) Total current (black line) and capacitive-contributed current (shadow area) of M1-250 electrode at 5 mV/s. (i) Relative contributions of different charge storage contribution of M1-250 electrode at various scan rates.

In order to characterize the changes in electronic states of M1 and M1-250, X-ray photoelectron spectroscopy (XPS) spectra were performed. As illustrated in the XPS survey spectra (Fig. S5), it can be determined that sample M1 contain Co 2p, C 1s, O 1s and N 1s, and sample M1-250 contain Co 2p, O 1s and C 1s. Among them, the presence of the N 1s peak in M1 is related with NH_4^+ adsorbed on the surface of M1 and the existence of the C 1s peak in M1-250 is due to the partial residual CoC_2O_4. In addition, Energy-dispersive X-ray spectroscopy (EDX) elemental mapping patterns of M1 and M1-250 further prove that the Co, C and O elements are uniformly distributed on the M1 surface, as well as the uniform distribution of Co and O elements on the M1-250 surface, as shown in Fig. S13 (Supporting information). Moreover, the high-resolution XPS spectrum of Co 2p for pre- and post-calcination samples (M1 and M1-250) is illustrated in Fig. 3f, in which M1 shows two major peaks at 797.4 and 781.4 eV, attributed to the characteristic Co $2p_{1/2}$ and Co $2p_{3/2}$ orbitals, respectively. The binding energy difference between Co $2p_{1/2}$ and Co $2p_{3/2}$ is 16 eV, which indicated that the Co(II) state in M1 [38]. After calcination, the deconvolution of Co $2p_{3/2}$ orbit in M1-250 illustrates two peaks at 782.1 and 780.9 eV, which corresponded to Co^{2+} and Co^{3+} cations, respectively. The other two typical peaks at 794.7 and 796.2 eV are attributed to Co $2p_{1/2}$ spin-orbit. Further fitting shows that the ratio of relative area of Co^{2+} to Co^{3+} in M1-250 is 2.31, which indicates that more exposed Co atoms were in $a + 2$ oxidation state on the M1-250 (CoC_2O_4/Co_3O_4) surface. The C 1s peaks for M1 centered at 284.8, 286.4, and 288.9 eV are ascribed to the C–C, C–O, and $C_2O_4^{2-}$ of CoC_2O_4, respectively (Fig. 3g) [41]. Compared to that of M1, the peak intensities of C–C, C–O and C=O in M1-250 are much lower, an indication that most of CoC_2O_4 are calcined to Co_3O_4. As illustrated in Fig. 3h, two characteristic peaks are located at 532.2 and 533.0 eV in the O 1s spectra for M1, which are attributed to C=O and O–H, respectively. After calcination, the peak at 529.4 eV correspond to Co-O in Co_3O_4 from M1-250.

In the three-electrode system, the electrochemical behaviors of M1, M1-200, M1-250, M1-300, M1-320 electrodes were measured in the aqueous electrolyte of 3.0 mol/L KOH, as displayed in Fig. 4. The cyclic voltammetry (CV) curves (Figs. S14a and S15 in Supporting information) at various scan rates from 5 mV/s to 100 mV/s of the as-obtained electrodes illustrates multiple redox peaks. As the scanning rate increasing, the peak values of cathodic and anodic change to lower and higher potentials, respectively, which is due to the electrode polarization and the decreased rate of ion diffusing at high scanning rates. The enclosed area from CV curve of the M1-250 is greater than that of the M1, M1-200, M1-300 and M1-320 (Fig. 4a), indicating the superiority of M1-250. The possible reaction process of energy storage for CoC_2O_4 and Co_3O_4 could be expressed as follows [42]:

$$CoC_2O_4{\cdot}2H_2O + OH^- \leftrightarrow Co(OH)C_2O_4{\cdot}2H_2O + e^- \quad (2)$$

$$Co_3O_4 + OH^- + H_2O \leftrightarrow 3CoOOH + e^- \quad (3)$$

$$CoOOH + OH^- \leftrightarrow CoO_2 + H_2O + e^- \quad (4)$$

The galvanostatic charge-discharge (GCD) curves of as-obtained electrodes were performed to comment the electrochemical prop-

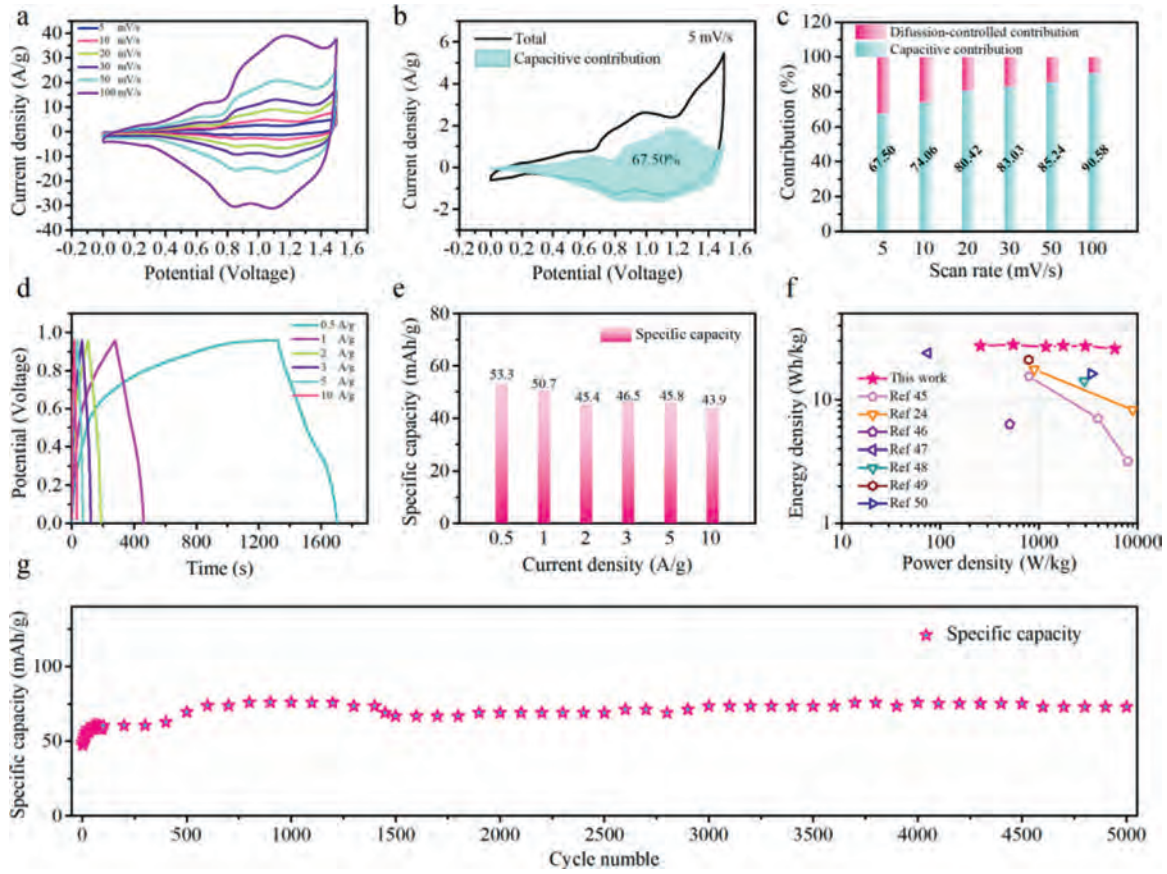

Fig. 5. Electrochemical performance of the M1-250//AC aqueous device: (a) CV curves at various scanning rates from 5 mV/s to 100 mV/s. (b) Total current (black line) and capacitive-contributed current (shadow area) at 5 mV/s. (c) Relative contributions of diffusion-controlled and capacitive processes at various scanning rates. (d) GCD curves and (e) specific capacity at various current densities from 0.5 A/g to 10 A/g. (f) Ragone plot for the assembled M1-250//AC aqueous device in comparison with some reported results. (g) Cycling performance of M1-250//AC at 5 A/g for 5000 cycles.

erties (Fig. 4b). It is found that the charge-discharge curve of the M1-250 electrode shows the longest charge-discharge time at 0.5 A/g. The specific capacities of the as-obtained electrodes (Fig. 4c) at different current density (0.5–10 A/g) are calculated from the corresponding GCD curves (Figs. S14b and S16 in Supporting information). The specific capacity of M1-250 (44.6 mAh/g) is much higher than that of M1 (13.4 mAh/g), M1-200 (18.5 mAh/g), M1-300 (27.0 mAh/g) and M1-320 (16.4 mAh/g) at 0.5 A/g (Table S1 in Supporting information). Interestingly, the M1-250 exhibits good rate capability by holding a capacity of 40.3 mAh/g at 10 A/g (90.3% capacity retention rate, as exhibited in Fig. 4d). Under open circuit condition, the conductivity of the as-prepared electrodes was measured by electrochemical impedance spectroscopy (EIS, shown in Fig. 4e). In high-frequency region, the nodal intercept of the horizontal axis in these EIS spectra represent the equivalent series resistance (R_s), of which M1-250 shows smaller R_s than M1-320. The slope of the straight line gives a reflection on the Warburg resistance (R_w) in low frequency zone [43]. And all electrodes show similar Warburg slope. However, M1-320 shows poor electrochemical properties, which might be related to the higher crystallinity and dense structure. In addition, the fitting equivalent circuit is simulated (Fig. S17 in Supporting information), and the corresponding parameter values are presented in Table S2 (Supporting information).

The detailed charge storage mechanism of M1-250 is initially investigated based on CV analyses (Fig. 4f). The overall stored charge includes diffusive and capacitive contribution. In terms of pseudocapacitive materials, it is the dominant process of capacitance when the redox reaction take place on the surface or the interlayer plane of the materials; While it is a dominant process of diffusion when the redox reaction occur inside the bulk active materials [21]. By analyzing the data with the following formula: $i = av^b$ (where a and b represent the variable parameters, i and v represent the peak current and scan rate, respectively), we can find that the b-values of anodic and cathodic peaks for M1-250 electrode are 0.81 and 0.89, respectively, implying that capacitive-controlled and diffusion process contributions simultaneously emerge in the charge storage process (Fig. 4g, the b-values of anodic and cathodic peaks for other electrodes are illustrated in Fig. S18 in Supporting information). Furthermore, based on the following equation: $i(V) = k_1v + k_2v^{1/2}$, the specific contribution of two processes can be calculated, where k_1v and $k_2v^{1/2}$ stand for capacitive-controlled process and diffusion-controlled process, respectively, and $i(V)$ is the response current. Fig. 4h illustrates the capacitive current (blue area) compared to the total current (black line) of the M1-250 electrode at 5 mV/s and the capacitive current contribution occupies about 56.27%. Moreover, the capacitive contribution of M1-250 increases from 56.27% to 84.92% when the scanning rate rises from 5 mV/s to 100 mV/s (Fig. 4i and Fig. S19 in Supporting information). Thus, the outstanding capacitive contribution of M1-250 suggests that the charge storage process at high scanning rate is mainly under the control of surface redox reaction.

In order to further evaluate the practical application value, an aqueous device was fabricated in an electrolyte of 3 mol/L KOH containing M1-250 (positive electrode material) and activated carbon (AC, negative electrode material). The specific capacitance of AC electrode at 1.0 A/g is 135 F/g (Fig. S20 in Supporting information). As displayed in Fig. 5a, the CV curves of the M1-250//AC

aqueous device at different scanning rates shows more than one set of redox peaks, which might be resulted from the surface redox reactions between Co^{2+} and Co^{3+}. In order to explore the hybrid kinetics of the M1-250//AC aqueous device, the divided capacitive current at 5 mV/s is displayed in Fig. 5b [44]. The contribution of the capacitive-controlled current enhances from 67.50 to 90.58% with the scanning rate rising from 5 mV/s to 100 mV/s (Figs. 5c and S21 in Supporting information).

The GCD curves of M1-250//AC aqueous device with different current density are displayed in Fig. 5d. As illustrated in Fig. 5e and Table S1, the calculated specific capacity values are 53.3 mAh/g at 0.5 A/g. The specific capacity retention is 82.3% with the increasing of current density from 0.5 A/g to 10 A/g (20 times). The good rate capability may benefit from the excellent ability of transporting of electron at high current density. However, the selection of higher voltage range could bring about the possible drawbacks of lower coulomb efficiency, shorter cycle life and lower capacity. Moreover, on the basis of GCD curves, the Ragone plots show the energy/power densities of M1-250//AC aqueous device in Fig. 5f, in which M1-250//AC aqueous device has a largest energy density of 27.9 Wh/kg when the power density is 550.7 W/kg, and it can be held at 25.9 Wh/kg with a higher power density of 5911.4 W/kg (Table S3 in Supporting information). Specifically, M1-250//AC aqueous device exhibits larger energy density than that of the reported devices, such as Co_3O_4//AC (15.4 Wh/kg at 800 W/kg) [45], α-Co/Ni$(OH)_2$@Co_3O_4-70//AC (23.9 Wh/kg at 75 W/kg) [46], Co-OA(S-3)//AC (17.7 Wh/kg at 900 W/kg) [24], Co_3O_4-NRs//AC (16.2 Wh/kg at 792.8 W/kg) [47], Co_3O_4-250//AC (14.2 Wh/kg at 2900 W/kg) [48], 3DPC/Co_3O_4//AC (21.1 Wh/kg at 790 W/kg) [49], CoC_2O_4//AC (16.2 Wh/kg at 3429 W/kg) [50]. Furthermore, it can be clearly seen from the Fig. 5g that there is an activation process in the initial 500 cycles, and the M1-250//AC aqueous device illustrates excellent cycling stability specifically reflected in a capacity holding 73.0 mAh/g after 5000 cycles at 5 A/g. Benefiting from the good conductivity of Co_3O_4, the M1-250//AC aqueous device has a low resistance (Fig. S22 in Supporting information), which may be related to the good conductivity of Co_3O_4. As displayed in Fig. S23 (Supporting information), the EIS spectra of the M1-250//AC aqueous device after 5000 cycles exhibits slightly larger R_s and R_w, compared with those before 5000 cycles.

In summary, we have utilized a facile and controllable approach to selectively prepare 2D nanostructured cobalt oxalate-based electrode materials, involving a precipitation step at room temperature mediated by changing the initial reactants ratio to decrease the concentration of $C_2O_4^{2-}$ion under the solvent of EG. By selecting EG as solvent to alter the factor of the electrolytic dissociation (α) and changing the ratio of the reactants, the morphology of $CoC_2O_4{\cdot}2H_2O$ was successfully tuned from 3D cuboid-like (M5) to 2D sheet-like (M1). Based on the low-temperature thermal transformation of M1, we obtained the 2D porous nanosheets M1-250 (Co_3O_4/CoC_2O_4 composite). In the three-electrode cell, the M1-250 electrode exhibited the largest specific capacity of 44.6 mAh/g at 0.5 A/g among the prepared electrodes. More importantly, the M1-250//AC aqueous device possessed good specific capacity of 53.3 mAh/g at 0.5 A/g A/g, and good capacity maintaining of 73.0 mAh/g after 5000 cycles. The preeminent electrochemical performance of M1-250 could be ascribed to the 2D sheet-like morphology and mesoporous structure, which provided big specific surface area and channels of ion transporting, leading to making full use of the accessible area to get high capacity. Besides, the presence of Co_3O_4 in CoC_2O_4 effectively provided more redox active sites, contributing to the increase of capacity. Better tuning and exploring of material morphologies will make sense to develop high-efficient and low-cost electrode materials for electrochemical energy storage device applications.

Declaration of competing interest

The authors declare that they have no known competing financial interests or personal relationships that could have appeared to influence the work reported in this paper.

Acknowledgments

This work was supported by the National Natural Science Foundation of China (No. U1904215), Natural Science Foundation of Jiangsu Province (No. BK20200044), Program for Young Changjiang Scholars of the Ministry of Education, China (No. Q2018270). We also acknowledge the Priority Academic Program Development of Jiangsu Higher Education Institutions and the technical support we received at the Testing Center of Yangzhou University.

Supplementary materials

Supplementary material associated with this article can be found, in the online version, at doi:10.1016/j.cclet.2021.10.075.

References

[1] T. Qiu, S. Gao, Z. Liang, et al., Angew. Chem. Int. Ed. 60 (2021) 17314–17336.
[2] Z. Liang, T. Qiu, S. Gao, R. Zhong, R. Zou, Adv. Energy Mater. 11 (2021) 2003410.
[3] S. Zheng, Q. Li, H. Xue, H. Pang, Q. Xu, Natl. Sci. Rev. 7 (2020) 305–314.
[4] C. Wang, X. Li, Q. Li, H. Pang, FlatChem. 16 (2019) 100107.
[5] T.T. Lv, Y.Y. Liu, H. Wang, et al., Chem. Eng. J. 411 (2021) 128533.
[6] Q. Zhang, Z. Liu, B. Zhao, et al., Energy Storage Mater. 16 (2019) 632–645.
[7] X. Qiu, N. Wang, Z. Wang, F. Wang, Y. Wang, Angew. Chem. Int. Ed. 60 (2021) 9610–9617.
[8] N. Han, M. Sun, Y. Zhou, et al., Adv. Mater. 33 (2021) 2005821.
[9] W.H. Lai, Y.X. Wang, Y. Wang, et al., Nat. Chem. 11 (2019) 695–701.
[10] Q. Li, X. Li, J. Gu, et al., Nano Res. 14 (2021) 1405–1412.
[11] Q. Li, N. Li, J. An, H. Pang, Inorg. Chem. Front. 7 (2020) 2089–2096.
[12] C. Gu, J. Li, G. Yang, et al., Chin. Chem. Lett. 31 (2020) 2263–2267.
[13] T. Lv, X. Luo, G. Yuan, S. Yang, H. Pang, Chem. Eng. J. 428 (2022) 131211.
[14] J. Li, Z. Liu, Q. Zhang, et al., Nano Energy 57 (2019) 22–33.
[15] S. Dai, Y. Bai, W. Shen, et al., J. Power Sources 482 (2021) 228915.
[16] Y. Zhao, S. Wei, K. Pan, et al., Chem. Eng. J. 421 (2021) 129645.
[17] Y.X. Pan, Z.Q. Sun, H.P. Cong, et al., Nano Res. 9 (2016) 1689–1700.
[18] Y. Li, Y. Xu, Y. Liu, H. Pang, Small 15 (2019) 1902463.
[19] X. Xiao, L. Zou, H. Pang, Q. Xu, Chem. Soc. Rev. 49 (2020) 301–331.
[20] H. Yin, Z. Tang, Chem. Soc. Rev. 45 (2016) 4873–4891.
[21] W. Chen, X. Yu, Z. Zhao, S. Ji, L. Feng, Electrochim. Acta 298 (2019) 313–320.
[22] C. Tan, H. Zhang, Chem. Soc. Rev. 44 (2015) 2713–2731.
[23] W.J. Ong, L.L. Tan, Y.H. Ng, S.T. Yong, S.P. Chai, Chem. Rev. 116 (2016) 7159–7329.
[24] T. Pu, J. Li, Y. Jiang, et al., Dalton Trans. 47 (2018) 9241–9249.
[25] L. Chen, Q. Zhang, H. Xu, et al., J. Mater. Chem. A 3 (2015) 1847–1852.
[26] R. Ma, T. Sasaki, Adv. Mater. 22 (2010) 5082–5104.
[27] X. Zhang, D. Han, X. Chen, et al., Acta Phys. Chim. Sin. 37 (2020) 2008055.
[28] S. Zheng, X. Guo, H. Xue, et al., Chem. Commun. 55 (2019) 10904–10907.
[29] J. Gu, Y. Xu, Q. Li, H. Pang, Chin. Chem. Lett. 32 (2021) 2017–2020.
[30] F. Sun, Q. Li, H. Xue, H. Pang, ChemElectroChem 6 (2019) 1273–1299.
[31] G. Yuan, S. Yu, J. Jie, et al., Chin. Chem. Lett. 31 (2020) 1941–1945.
[32] J. Cui, J. Zheng, W. Qiao, X. Wan, J. Colloid Interface Sci. 326 (2008) 267–274.
[33] L. Ni, C. Shen, G. Yong, Mater. Chem. Phys. 205 (2018) 278–282.
[34] R.R. Sever, T.W. Root, J. Phys. Chem. B 107 (2003) 4080–4089.
[35] G. Zhang, L. Jin, R. Zhang, et al., Coord. Chem. Rev. 439 (2021) 213915.
[36] Y.F. Yang, S.B. Jin, Q.C. Jiang, CrystEngComm 15 (2013) 852–855.
[37] A.M. Cao, J.S. Hu, H.P. Liang, L.J. Wan, Angew. Chem. Int. Ed. 44 (2005) 4391–4395.
[38] Y. Wei, X. Ren, H. Ma, et al., Chem. Commun. 54 (2018) 1533–1536.
[39] S. Ye, J. Wang, J. Hu, et al., ACS Catal. 11 (2021) 6104–6112.
[40] X. Yin, C. Zhi, W. Sun, L.P. Lv, Y. Wang, J. Mater. Chem. A 7 (2019) 7800–7814.
[41] Y. Zhang, C. Wang, Y. Dong, R. Wei, J. Zhang, Chem. Eur. J. 27 (2021) 993–1001.
[42] T. Chen, Z. Liu, H. Fan, L. Guo, X. Tao, J. Alloy. Compd. 808 (2019) 151722.
[43] Z. Liu, A. Li, Y. Qiu, et al., J. Colloid Interface Sci. 592 (2021) 455–467.
[44] L. Li, W. Liu, K. Jiang, et al., Nano-Micro Lett 13 (2021) 100.
[45] Y. Jiang, L. Chen, H. Zhang, et al., Chem. Eng. J. 292 (2016) 1–12.
[46] Y. Bao, Y. Deng, M. Wang, et al., Appl. Surf. Sci. 504 (2020) 144395.
[47] T. Liu, L. Zhang, W. You, J. Yu, Small 14 (2018) 1702407.
[48] G. Cheng, T. Kou, J. Zhang, et al., Nano Energy 38 (2017) 155–166.
[49] S. Li, K. Yang, P. Ye, et al., Appl. Surf. Sci. 503 (2020) 144090.
[50] G. Cheng, C. Si, J. Zhang, et al., J. Power Sources 312 (2016) 184–191.